Science Advances

AAAS

Supplementary Materials for

Layer-resolved ultrafast extreme ultraviolet measurement of hole transport in a Ni-TiO$_2$-Si photoanode

Scott K. Cushing, Ilana J. Porter, Bethany R. de Roulet, Angela Lee, Brett M. Marsh, Szilard Szoke, Mihai E. Vaida, Stephen R. Leone*

*Corresponding author. Email: srl@berkeley.edu

This PDF file includes:

Supplementary Methods
Fig. S1 to S6
References

Supplementary Methods: Theoretical and Computational Details.

Silicon L$_{2,3}$ Edge The ground state Si XUV absorption was predicted using the OCEAN code (Obtaining Core-level Excitations using Ab initio methods and the NIST BSE solver). The energy-dependent broadening is included using a Drude-Lindhard single-plasmon pole model for the electron loss function. The ground state electron densities and wave-functions are calculated at the density functional level (DFT) using Quantum-ESPRESSO (*39*). The local density approximation (LDA) using a norm-conserving generalized gradient approximation (GGA) Perdew-Burke-Ernzerhof pseudopotential is used to calculate the density of states with a converged k-point mesh of 20x20x20 points and a plane wave cutoff of 100 Ry. The lattice constant is converged at 5.46 Angstroms. Projector augmented wave (PAW) reconstructed wave functions are used for calculating the core-level transition matrix elements. A real-space random phase approximation is used to estimate the dielectric screening inside a sphere around the atom, while the Levine-Louie dielectric function is used outside this sphere (*40, 41*). The Bethe-Salpeter (BSE) equation is then used to calculate the final electron-hole states.

In the BSE-DFT calculation, the final states are converged at k-point meshes of 8x8x8 and using a total number of bands of 100. The projector augmented wave states are converged at k-point meshes of 2x2x2 and using a total number of bands of 200. The SCF mixing is taken as 0.7 with 250 iterations used. The BSE mesh is 6x6x6, with a cut-off radius of 8.0 Bohr. The projector augmented wave shell radius is taken as 8.0 Bohr with a 0.8 scaling factor of the slater G parameter. The dielectric constant of silicon is taken as 11.7. XUV dipole orientations along the [100] and [110] directions are calculated, but within the experimental broadening, little difference is found in the final predicted x-ray absorption. A comparison of this fit with the ground state absorbance is shown in Fig. S3A.

The excited state changes to the Si $L_{2,3}$ edge are known to originate in a variety of electronic and structural dynamics. A simplified version of the model to extract electron energies, hole energies, and the temperature of the lattice is used (*42*). Specifically, the differential absorption features above 101.5 eV are mainly from structural distortions related to heating the lattice, similar to what is measured in EXAFS. A multivariate regression is used to extract the amplitude of the initial and final thermal contributions to the differential absorption. The amplitude of the structural dynamics above 101.5 eV is multiplied with the full spectrum and subtracted from each time point. The residual, filtered by the known energy ranges of the electron and hole contributions, represents the electron and hole energy as a function of time. The relative amplitudes are calculated by integrating over these ranges, giving the values shown in the main text Fig. 3A. All of the fitted parameters, not just the electron and hole populations shown in the main text, are included in Fig. S5A and S5B for the Si in the junction and alone, respectively. Differential absorptions for these two samples can be found in the main text Fig. 1C for the Si in the junction and Fig. S1A for the Si alone.

Nickel $M_{2,3}$ Edge The Ni $M_{2,3}$ edge is modeled using the many-body approach of Ohtaka and Tanabe (*43*). This model is derived by summing over the transition probabilities for all possible final states, assuming parabolic bands and a scattering potential caused by the core hole. The resultant ground state absorption includes the "orthogonality catastrophe" or "white line" effect common to the x-ray absorption of metals,

$$I'(\omega^*) = \frac{1}{D}\left[\frac{D}{2\pi T}\right]^{\zeta_0} \mathrm{Re}\left[e^{i\left(\pi/2\right)(\zeta_0-1)} \frac{\Gamma\left(\frac{1-\zeta_0}{2}-\frac{i\omega^*}{2\pi T}\right)\Gamma(\zeta_0)}{\Gamma\left(\frac{1+\zeta_0}{2}-\frac{i\omega^*}{2\pi T}\right)}\right] \tag{1}$$

Where I' is intensity, $\omega^* = (\omega - \omega_{th})$, which is the frequency with respect to the edge onset frequency ω_{th} as given by the Fermi level of the metal, D is the bandwidth or energy difference between the Fermi level and conduction band upper edge, T is temperature, and ζ_0 is the phase shift of the Fermi sea caused by scattering with the core-hole contact potential. The ground state Ni $M_{2,3}$ edge is modeled by fitting the values of ω_{th}, T, D and ζ_0 to the ground state absorption spectrum. To account for the spin-orbit splitting of the Ni 3p level, the total spectrum is modeled as the sum of two of such peaks, keeping all four fit variables constant, and fitting the spin-orbit splitting energy and peak ratio. A comparison of this fit with the measured spectrum is shown in Fig. S3. Since the phase factor ζ_0 depends on the energetics of the electrons filling the Fermi sea, it contains no new information other than ω and T.

To model the differential absorption spectrum of the excited state Ni $M_{2,3}$ edge, the modeled ground state spectrum for both spin-orbit components is subtracted from the modeled excited state fit, in which all variables are held constant from the ground state calculation except ω_{th}, T, and ζ_0. Since Ni is not a free-electron metal, the magnitudes of D, T and ζ_0 in the ground state are nonphysical. The magnitude of the excited state changes, however, prove experimentally accurate. For example, the temperature shift matches the predicted value for the given carrier concentration and heat capacity. The change in Fermi level matches the number of carriers photoexcited in the Ni. The differential absorption spectrum of the photoexcited Ni in the junction can be seen in the main text Fig. 1C, and the differential absorption of the Ni alone is shown in Fig. S1B. A comparison of the ground state absorbances of these two samples is found in Fig. S2A. All fitted parameters are shown in Fig. S5C and S5D for the Ni in the junction and alone, respectively. A comparison of the fitted Fermi level for the junction and alone sample are in the top panel of the main text Fig. 3B.

Titanium M$_{2,3}$ Edge Similar to the Si L$_{2,3}$ edge, the ground state absorption of the TiO$_2$ at

the Ti M$_{2,3}$ edge is first modelled using the OCEAN code. The DFT k-point mesh was

6x6x4 with a lattice constant of a=3.75 and c=9.38 Angstroms. The local density

approximation (LDA) is used with a norm-conserving Perdew-Wang pseudopotential

since OCEAN cannot use LDA+U or hybrid functionals. A plane wave cut-off of 100 Ry

was used for the pseudopotential. In the BSE calculation, the final states are converged at

k-point meshes of 6x6x4 and using a total number of bands of 50. The projector

augmented wave states are converged at k-point meshes of 2x2x2 and using a total

number of bands of 100. The BSE mesh is 4x4x4, with a cut-off radius of 4.0 Bohr. The

projector augmented wave shell radius is taken as 4.0 Bohr with a 0.8 scaling factor of the

slater G parameter. The dielectric constant of TiO$_2$ is taken as 20 to approximate

amorphous TiO$_2$. XUV dipole alignments along the [100] and [111] directions are

calculated, but within the experimental broadening and amorphous TiO$_2$ layer, little

difference is found in the final predicted x-ray absorption. An energy-dependent

broadening was included by using a separate Lorentzian for each atomic multiplet split

peak. The value of the broadening was 3 eV except for the central peak, which was 5 eV.

This modeled spectrum is compared to the measured static absorbance in Fig. S3C.

The atomic multiplet splitting in the metal oxide means that only charge state and a

change in broadening can be extracted as a function of time. This is achieved by fitting a

global Lorentzian broadening and an energetic shift to the ground state absorption, and

then subtracting the unmodified ground state absorption to calculate the differential

absorption. These fitted parameters are shown in Fig. S5E for the TiO$_2$ in the junction and

in Fig. S5F for the TiO$_2$ alone. Differential absorption following photoexcitation for the

TiO2 in the junction and alone can be found in the main text Fig. 1C and Fig. S1C,

respectively. A comparison of the fitted edge shift for both samples is shown in the bottom panel of the main text Fig. 3B.

Drift-Diffusion Calculation The calculation of the band bending and electric field inside the Ni-TiO$_2$-Si junction shown in Figure 1A was performed using the AFORS-HET (Automat FOR Simulation of HETerostructures) open access program (*27, 44*). This simulation tool numerically solves the one-dimensional Poisson's equations for semiconductors to find the electric field, charge and current densities for a specified series of layers with given boundary conditions. Then, the resultant field and densities are applied to the semiconductor equations iteratively until a steady-state solution is reached. These so-called semiconductor equations are

$$\frac{\partial D}{\partial x} = +q(p - n + \rho + N_D - N_A) \tag{2}$$

$$\frac{\partial J_n}{\partial x} = -q(G - R_n) \tag{3}$$

$$\frac{\partial J_p}{\partial x} = +q(G - R_p) \tag{4}$$

where D is the field that displaces charges, p is the hole density, n is the electron density, ρ is the density of interband traps, N is the acceptor/donor concentration, J is the current density for electrons (n) or holes (p), G is the optical generation rate, and R is the recombination rate for electrons (n) or holes (p). The program models recombination using the Shockley-Read-Hall formalism, and carrier densities are calculated with Boltzmann statistics.

Many different boundary conditions can be applied to the system, including a constant voltage at one of the contacts or a constant boundary current. Additionally, interfaces between the layers can have their own specified boundary conditions. The general form is:

$$\varphi(x) = \phi_j - \phi_i - V \tag{5}$$

$$J_n(x) = -q \cdot S_n^i(n(x) - n_{eq}(x)) \tag{6}$$

$$J_p(x) = +q \cdot S_p^i\big(p(x) - p_{eq}(x)\big) \tag{7}$$

where φ is the potential at position x, ϕ_i and ϕ_j are the work functions of the front and back layers, V is an optional applied voltage, S is the recombination velocity of electrons (n) or holes (p) at layer i, n_{eq} is the equilibrium electron density, and p_{eq} is the equilibrium hole density. The semiconductor work functions are calculated by the AFORS-HET program from the electron affinity, band gap, and doping levels provided by the user. For the calculation of the Ni-TiO$_2$-Si junction band diagram in this study, the electron affinity of the p-Si is 4.05 eV, the electron affinity of the n-TiO$_2$ is 4.0 eV, the work function of the Ni is 5.1 eV, and the boundary voltages are set to zero.
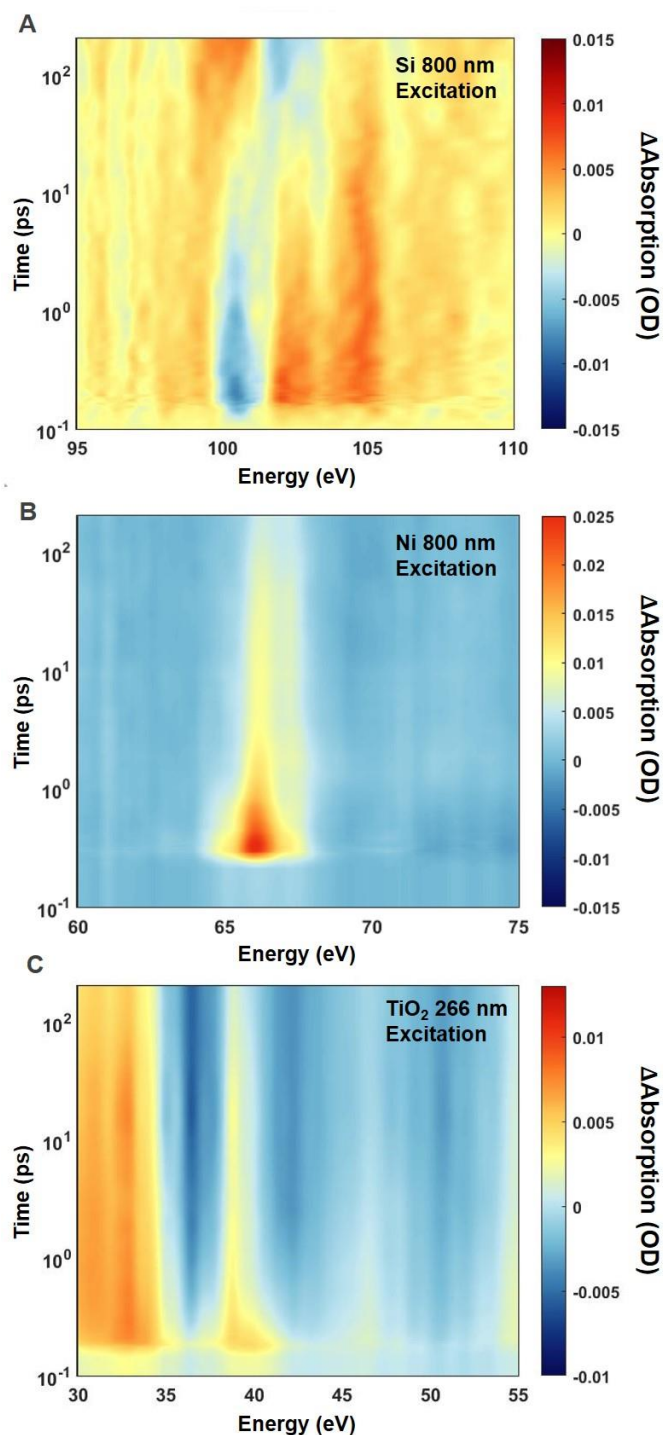
Fig. S1. Transient differential data for reference samples. The differential XUV absorption is shown on a negative (blue) to positive (red) colormap. The timescale is logarithmic and offset by 100 fs for visualization. (**A**) Differential absorption for Si alone with 800 nm light. (**B**) Differential absorption for photoexcitation of Ni alone with 800 nm light. (**C**) Differential absorption for 266 nm photoexcitation of TiO_2 alone.
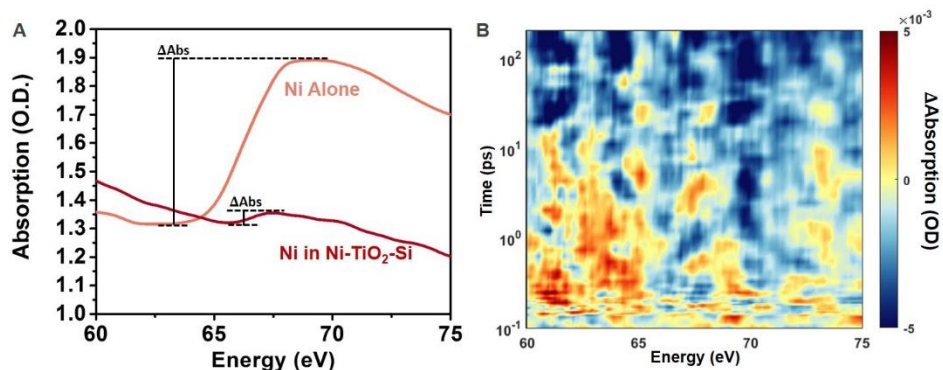
Fig. S2. Ni in Ni-TiO$_2$-Si versus Ni alone. (**A**) The absorption of the Ni in the junction is over ten times less than the Ni alone film when measured from pre-edge dip to peak (ΔAbs). The lines have been vertically offset for comparison. (**B**) The differential absorption following 800 nm excitation of a thin Ni sample with similar thickness to the Ni in the junction. This thin Ni film has no signal within a few mOD noise level. The thicker Ni alone sample has an ~25 mOD signal as seen in Fig. S1B.
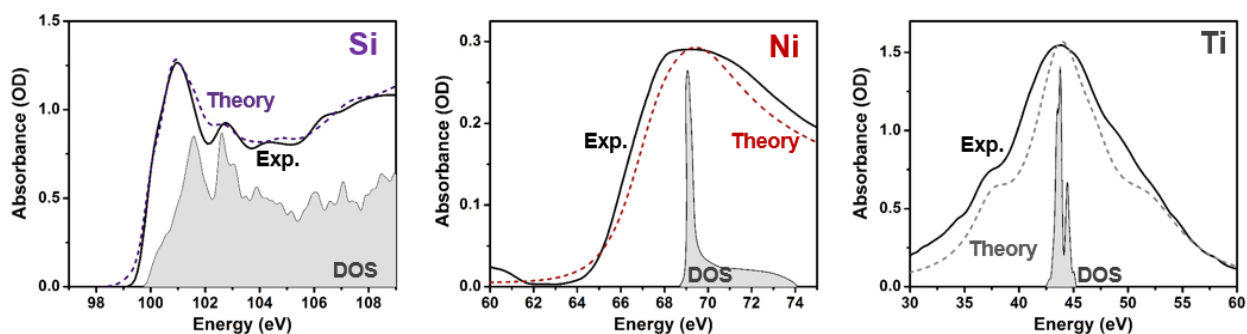

Fig. S3. Modeling the XUV ground and excited state absorption. (**A-C**) The experimental XUV absorption of each element (solid lines) is compared to the BSE-DFT calculation (dashed lines) and the approximate valence density of states (DOS) from DFT for each material. How well the valence charge density screens the core-hole perturbation from the XUV excitation determines to what degree the XUV spectrum reflects the valence density of states.
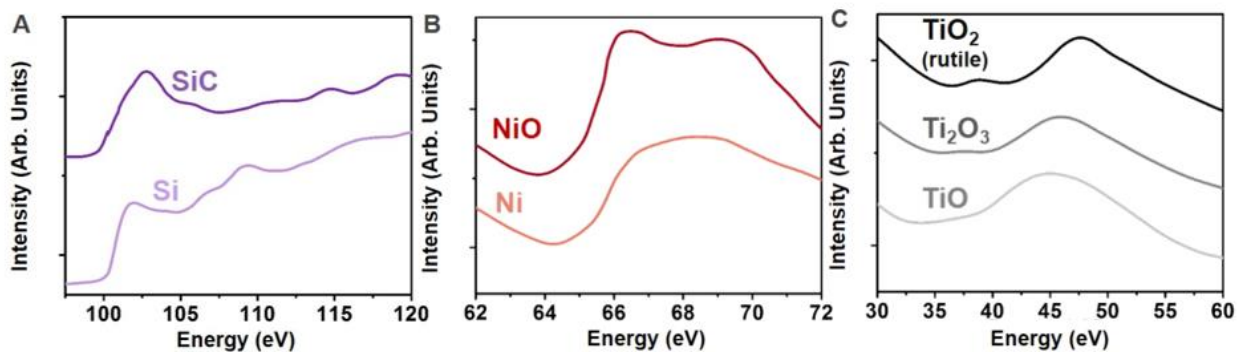
Fig. S4. Comparison of EELS absorption in the XUV range for different compounds.
XUV absorption data from synchrotron sources is not readily available, so the electron energy loss (EELS) absorption is shown for each element (*45*). The EELS absorption process involves a one-electron excitation instead of a one-photon excitation (**A**) For Si, the core-hole is well screened, and the peak structure and energy are more representative of the underlying band structure than the oxidation state (compare Si and SiC). (**B**) For Ni, the edge rise is sensitive to the number of holes or oxidation state. When electrons are removed in the metal, the Fermi level changes, and the edge shifts to lower energy while increasing in absorption. (**C**) For Ti, the broad absorption and appearance of multiplet split peaks is sensitive to the oxidation state.
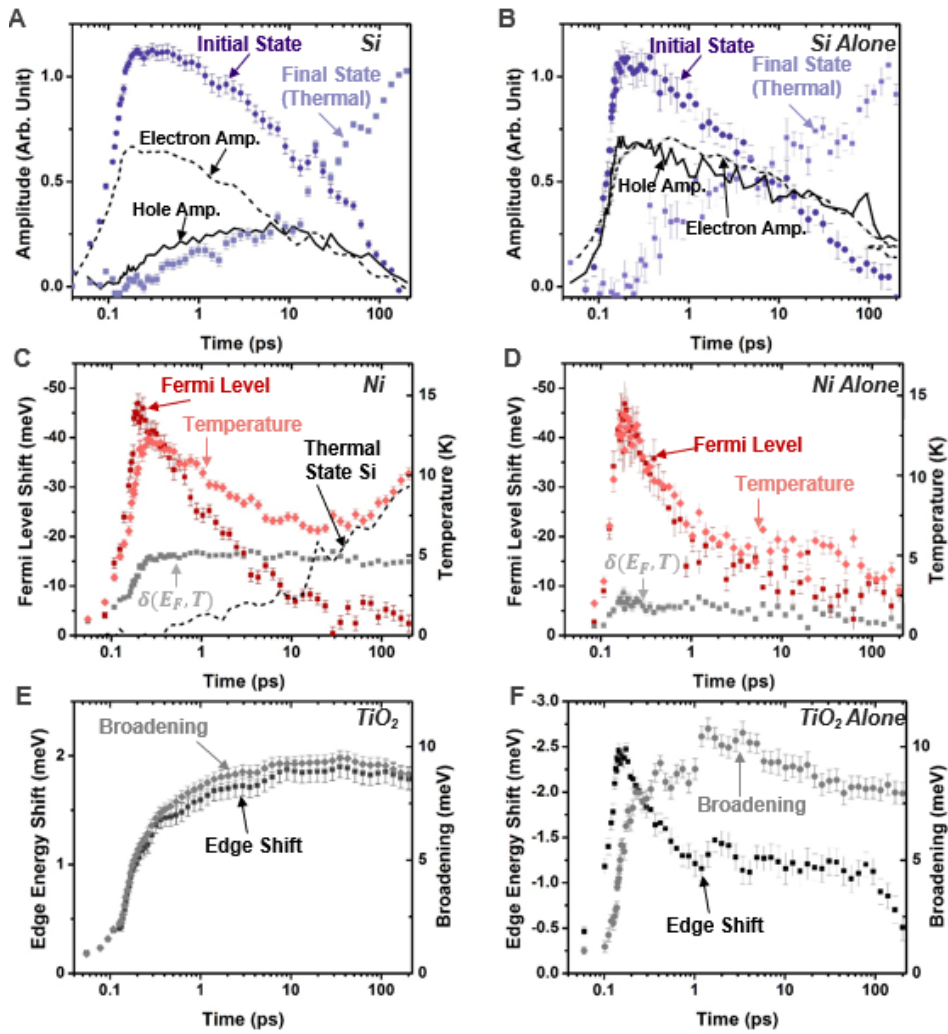
Fig. S5. All fit parameters for each XUV edge as a function of time. (**A**) For Si in the junction, the amplitude of the initial and final states used in the multivariate regression are shown as the dark purple circles and light purple squares, respectively. The final state represents a heated lattice. The electron and hole features' spectral amplitudes after removal of the final thermal state are shown as the dashed and solid black lines, respectively. (**B**) The same as in Panel A, but for Si alone. (**C**) For Ni in the junction, the fit Fermi level (red circles), temperature in the Fermi-Dirac distribution (light red diamonds), and the phase factor (gray squares) which is co-dependent on the Fermi level and temperature are shown. The final thermal state from the Si fit is shown as a dashed black line. (**D**) The same as in panel C but for Ni alone. (**E**) For TiO_2, the fit broadening (grey diamonds) and edge shift (black squares) of the Ti edge. The error bars correspond

to the non-linear-fit standard error from a robust-fit weighted by the experimental

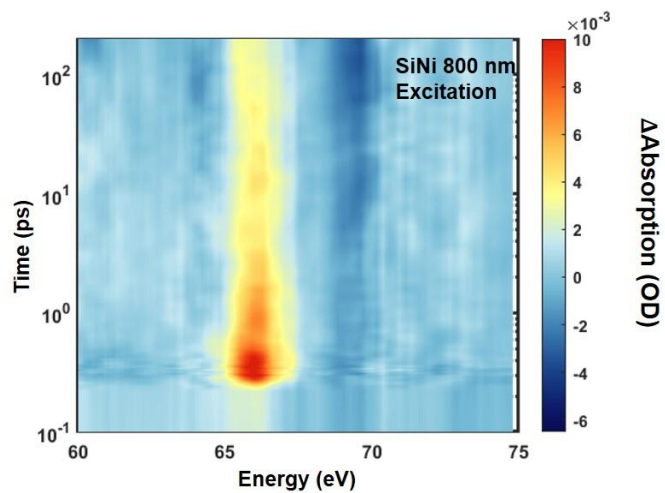uncertainty. (**F**) The same as in Panel E but for TiO_2 alone.

Fig. S6. Transient differential data for 800 nm photoexcitation of Si-Ni as measured at the Ni edge.

REFERENCES AND NOTES

1. M. A. Green, Y. Hishikawa, E. D. Dunlop, D. H. Levi, J. Hohl-Ebinger, A. W. Y. Ho-Baillie, Solar cell efficiency tables (version 52). *Prog. Photovolt.* **26**, 427–436 (2018).

2. J. W. Ager, M. R. Shaner, K. A. Walczak, I. D. Sharp, S. Ardo, Experimental demonstrations of spontaneous, solar-driven photoelectrochemical water splitting. *Energ. Environ. Sci.* **8**, 2811–2824 (2015).

3. W.-H. Cheng, M. H. Richter, M. M. May, J. Ohlmann, D. Lackner, F. Dimroth, T. Hannappel, H. A. Atwater, H.-J. Lewerenz, Monolithic photoelectrochemical device for direct water splitting with 19% efficiency. *ACS Energy Lett.* **3**, 1795–1800 (2018).

4. A. G. Aberle, Surface passivation of crystalline silicon solar cells: A review. *Prog. Photovolt.* **8**, 473–487 (2000).

5. S. Hu, M. R. Shaner, J. A. Beardslee, M. Lichterman, B. S. Brunschwig, N. S. Lewis, Amorphous TiO_2 coatings stabilize Si, GaAs, and GaP photoanodes for efficient water oxidation. *Science* **344**, 1005–1009 (2014).

6. A. G. Scheuermann, J. P. Lawrence, K. W. Kemp, T. Ito, A. Walsh, C. E. D. Chidsey, P. K. Hurley, P. C. McIntyre, Design principles for maximizing photovoltage in metal-oxide-protected water-splitting photoanodes. *Nat. Mater.* **15**, 99–105 (2016).

7. L. Pan, J. H. Kim, M. T. Mayer, M.-K. Son, A. Ummadisingu, J. S. Lee, A. Hagfeldt, J. Luo, M. Grätzel. Boosting the performance of Cu_2O photocathodes for unassisted solar water splitting devices. *Nat. Catal.* **1**, 412–420 (2018).

8. D. Bae, B. Seger, P. C. K. Vesborg, O. Hansen, I. Chorkendorff, Strategies for stable water splitting *via* protected photoelectrodes. *Chem. Soc. Rev.* **46**, 1933–1954 (2017).

9. J. Gu, Y. Yan, J. L. Young, K. X. Steirer, N. R. Neale, J. A. Turner, Water reduction by a p-$GaInP_2$ photoelectrode stabilized by an amorphous TiO_2 coating and a molecular cobalt catalyst. *Nat. Mater.* **15**, 456–460 (2016).

10. G. Zeng, J. Qiu, Z. Li, P. Pavaskar, S. B. Cronin, CO_2 reduction to methanol on TiO_2-passivated GaP photocatalysts. *ACS Catal.* **4**, 3512–3516 (2014).

11. E. Kalamaras, M. M. Maroto-Valer, M. Shao, J. Xuan, H. Wang, Solar carbon fuel via photoelectrochemistry. *Catal. Today* **317**, 56–75 (2018).

12. H. H. Pham, L.-W. Wang, Oxygen vacancy and hole conduction in amorphous TiO_2. *Phys. Chem. Chem. Phys.* **17**, 541–550 (2015).

13. S. Hu, M. H. Richter, M. F. Lichterman, J. Beardslee, T. Mayer, B. S. Brunschwig, N. S. Lewis, Electrical, photoelectrochemical, and photoelectron spectroscopic investigation of the interfacial transport and energetics of amorphous TiO_2/Si heterojunctions. *J. Phys. Chem. C* **120**, 3117–3129 (2016).

14. L. Young, K. Ueda, M. Gühr, P. H. Bucksbaum, M. Simon, S. Mukamel, N. Rohringer, K. C. Prince, C. Masciovecchio, M. Meyer, A. Rudenko, D. Rolles, C. Bostedt, M. Fuchs, D. A. Reis, R. Santra, H. Kapteyn, M. Murnane, H. Ibrahim, F. Légaré, M. Vrakking, M. Isinger, D. Kroon, M. Gisselbrecht, A. L'Huillier, H. J. Wörner, S. R. Leone, Roadmap of ultrafast x-ray atomic and molecular physics. *J. Phys. B At. Mol. Opt. Phys.* **51**, 032003 (2018).

15. P. M. Kraus, M. Zürch, S. K. Cushing, D. M. Neumark, S. R. Leone, The ultrafast x-ray spectroscopic revolution in chemical dynamics. *Nat. Rev. Chem.* **2**, 82–94 (2018).

16. T. Brabec, F. Krausz, Intense few-cycle laser fields: Frontiers of nonlinear optics. *Rev. Mod. Phys.* **72**, 545–591 (2000).

17. J. J. Rehr, Failure of the quasiparticle picture of x-ray absorption? *Found. Phys.* **33**, 1735–1742 (2003).

18. L. Campbell, L. Hedin, J. J. Rehr, W. Bardyszewski, Interference between extrinsic and intrinsic losses in x-ray absorption fine structure. *Phys. Rev. B* **65**, 064107 (2002).

19. M.-F. Lin, M. A. Verkamp, J. Leveillee, E. S. Ryland, K. Benke, K. Zhang, C. Weninger, X. Shen, R. Li, D. Fritz, U. Bergmann, X. Wang, A. Schleife, J. Vura-Weis, Carrier-specific femtosecond XUV transient absorption of PbI_2 reveals ultrafast nonradiative recombination. *J. Phys. Chem. C* **121**, 27886–27893 (2017).

20. M. Zürch, H.-T. Chang, L. J. Borja, P. M. Kraus, S. K. Cushing, A. Gandman, C. J. Kaplan, M. H. Oh, J. S. Prell, D. Prendergast, C. D. Pemmaraju, D. M. Neumark, S. R. Leone, Direct and simultaneous observation of ultrafast electron and hole dynamics in germanium. *Nat. Commun.* **8**, 15734 (2017).

21. S. Biswas, J. Husek, S. Londo, L. R. Baker, Ultrafast electron trapping and defect-mediated recombination in NiO probed by femtosecond extreme ultraviolet reflection–absorption spectroscopy. *J. Phys. Chem. Lett.* **9**, 5047–5054 (2018).

22. S. K. Cushing, A. Lee, I. J. Porter, L. M. Carneiro, H.-T. Chang, M. Zürch, S. R. Leone, Differentiating photoexcited carrier and phonon dynamics in the Δ, L, and Γ valleys of Si(100) with transient extreme ultraviolet spectroscopy. *J. Phys. Chem. C* **123**, 3343–3352 (2019).

23. M. T. McDowell, M. F. Lichterman, A. I. Carim, R. Liu, S. Hu, B. S. Brunschwig, N. S. Lewis, The influence of structure and processing on the behavior of TiO_2 protective layers

for stabilization of n-Si/TiO₂/Ni photoanodes for water oxidation. *ACS Appl. Mater. Interfaces* **7**, 15189–15199 (2015).

24. M. E. Vaida, S. R. Leone, Femtosecond extreme ultraviolet photoemission spectroscopy: Observation of ultrafast charge transfer at the n-TiO₂/p-Si(100) interface with controlled TiO₂ oxygen vacancies. *J. Phys. Chem. C* **120**, 2769–2776 (2016).

25. S. K. Cushing, F. Meng, J. Zhang, B. Ding, C. K. Chen, C.-J. Chen, R.-S. Liu, A. D. Bristow, J. Bright, P. Zheng, N. Wu, Effects of defects on photocatalytic activity of hydrogen-treated titanium oxide nanobelts. *ACS Catal.* **7**, 1742–1748 (2017).

26. J. Nowotny, M. A. Alim, T. Bak, M. A. Idris, M. Ionescu, K. Prince, M. Z. Sahdan, K. Sopian, M. A. M. Teridi, W. Sigmund, Defect chemistry and defect engineering of TiO₂-based semiconductors for solar energy conversion. *Chem. Soc. Rev.* **44**, 8424–8442 (2015).

27. R. Varache, C. Leendertz, M. E. Gueunier-Farret, J. Haschke, D. Muñoz, L. Korte, Investigation of selective junctions using a newly developed tunnel current model for solar cell applications. *Sol. Energy Mater. Sol. Cells* **141**, 14–23 (2015).

28. K. A. Nagamatsu, S. Avasthi, G. Sahasrabudhe, G. Man, J. Jhaveri, A. H. Berg, J. Schwartz, A. Kahn, S. Wagner, J. C. Sturm, Titanium dioxide/silicon hole-blocking selective contact to enable double-heterojunction crystalline silicon-based solar cell. *Appl. Phys. Lett.* **106**, 123906 (2015).

29. Q. Zhang, K. Zhao, J. Li, M. Chini, Y. Cheng, Y. Wu, E. Cunningham, Z. Chang, Suppression of driving laser in high harmonic generation with a microchannel plate. *Opt. Lett.* **39**, 3670–3673 (2014).

30. S. K. Cushing, M. Zürch, P. M. Kraus, L. M. Carneiro, A. Lee, H.-T. Chang, C. J. Kaplan, S. R. Leone, Hot phonon and carrier relaxation in Si(100) determined by transient extreme ultraviolet spectroscopy. *Struct. Dyn.* **5**, 054302 (2018).

31. J. M. Dorkel, P. Leturcq, Carrier mobilities in silicon semi-empirically related to temperature, doping and injection level. *Solid State Electron.* **24**, 821–825 (1981).

32. L. Gao, Q. Li, H. Chen, S. Hayase, T. Ma, In situ fabrication of nanoepitaxial TiO₂ protection layer on Si substrate: Hole chemical conduction instead of tunneling effect. *Sol. RRL.* **1**, 1700064 (2017).

33. M. Schultze, E. M. Bothschafter, A. Sommer, S. Holzner, W. Schweinberger, M. Fiess, M. Hofstetter, R. Kienberger, V. Apalkov, V. S. Yakolev, M. I. Stockman, F. Krausz, Controlling dielectrics with the electric field of light. *Nature* **493**, 75–78 (2012).

34. A. Schiffrin, T. Paasch-Colberg, N. Karpowicz, V. Apalkov, D. Gerster, S. Mühlbrandt, M. Korbman, J. Reichert, M. Schultze, S. Holzner, J. V. Barth, R. Kienberger, R. Ernstorfer, V.

S. Yakovlev, M. I. Stockman, F. Krausz, Optical-field-induced current in dielectrics. *Nature* **493**, 70–74 (2012).

35. M. Lenzner, J. Krüger, S. Sartania, Z. Cheng, C. Spielmann, G.Mourou, W. Kautek, F. Krausz, Femtosecond optical breakdown in dielectrics. *Phys. Rev. Lett.* **80**, 4076–4079 (1998).

36. C. Neusel, G. A. Schneider, Size-dependence of the dielectric breakdown strength from nano- to millimeter scale. *J. Mech. Phys. Solids* **63**, 201–213 (2014).

37. V. Titova, D. Startsev, J. Schmidt, Electron-selective atomic-layer-deposited TiO_x layers: Impact of post-deposition annealing and implementation into n-type silicon solar cells. *AIP Conf. Proc.* **1999**, 040022 (2018).

38. O. Kfir, E. Bordo, G. Ilan Haham, O. Lahav, A. Fleischer, O. Cohen, In-line production of a bi-circular field for generation of helically polarized high-order harmonics. *Appl. Phys. Lett.* **108**, 211106 (2016).

39. P. Giannozzi, S. Baroni, N. Bonini, M. Calandra, R. Car, C. Cavazzoni, D. Ceresoli, G. L. Chiarotti, M. Cococcioni, I. Dabo, A. D. Corso, S. de Gironcoli, S. Fabris, G. Fratesi, R. Gebauer, E. Gerstmann, C. Gougoussis, A. Kokalj, M. Lazzeri, L. Martin-Samos, N. Marzari, F. Mauri, R. Mazzarello, S. Paolini, A. Pasquarello, L. Paulatto, C. Sbraccia, S. Scandolo, G. Sclauzero, A. P. Seitsonen, A. Smogunov, P. Umari, R. M. Wentzcovitch, Quantum ESPRESSO: A modular and open-source software project for quantum simulations of materials. *J. Phys. Condens. Matter* **21**, 395502 (2009).

40. E. L. Shirley, Local screening of a core hole: A real-space approach applied to hafnium oxide. *Ultramicroscopy* **106**, 986–993 (2006).

41. Z. H. Levine, S. G. Louie, New model dielectric function and exchange-correlation potential for semiconductors and insulators. *Phys. Rev. B* **25**, 6310–6316 (1982).

42. C. C. Evans, J. D. B. Bradley, E. A. Martí-Panameño, E. Mazur, Mixed two- and three-photon absorption in bulk rutile (TiO_2) around 800 nm. *Opt. Express* **20**, 3118–3128 (2012).

43. K. Ohtaka, Y. Tanabe, Golden-rule approach to the soft-x-ray-absorption problem. III. The temperature dependence. *Phys. Rev. B* **30**, 4235–4258 (1984).

44. A. Froitzheim, R. Stangl, L. Elstner, M. Kriegel, W. Fuhs, AFORS-HET: A computer-program for the simulation of heterojunction solar cells to be distributed for public use, *in Proceedings of 3rd World Conference on Photovoltaic Energy Conversion, 2003* (IEEE, 2003) pp. 279–282.

45. L. A. J. Garvie, A. J. Craven, R. Brydson, Use of electron-energy loss near-edge fine structure in the study of minerals. *Am. Mineral.* **79**, 411–425 (1994).